



ELSEVIER

Nuclear Instruments and Methods in Physics Research A 444 (2000) 569–583

**NUCLEAR
INSTRUMENTS
& METHODS
IN PHYSICS
RESEARCH**
Section A

www.elsevier.nl/locate/nima

Cryogenic cavity detector for a large-scale cold dark-matter axion search

H. Peng^a, S. Asztalos^{a,*}, E. Daw^a, N.A. Golubev^b, C. Hagmann^c, D. Kinion^c,
J. LaVeigne^d, D.M. Moltz^e, F. Nezzrick^f, J. Powell^c, L.J. Rosenberg^a, P. Sikivie^d,
W. Stoeffl^c, N.S. Sullivan^d, D.B. Tanner^d, M.S. Turner^{g,h}, K. van Bibber^c

^a*Department of Physics and Laboratory For Nuclear Science, Massachusetts Institute of Technology, 77 Massachusetts Avenue, Cambridge, MA 02139, USA*

^b*Institute for Nuclear Research of the Russian Academy of Science, 60th October Anniversary Prospekt 7a, 117312 Moscow, Russia*

^c*Lawrence Livermore National Laboratory, 7000 East Avenue, Livermore, CA 94550, USA*

^d*Department of Physics, University of Florida, Gainesville, FL 32611, USA*

^e*Lawrence Berkeley National Laboratory, 1 Cyclotron Road, Berkeley, CA 94720, USA*

^f*Fermi National Accelerator Laboratory, Batavia, IL 60510-0500, USA*

^g*Theoretical Astrophysics, Fermi National Accelerator Laboratory, Batavia, IL 60510-0500, USA*

^h*Department of Astronomy & Astrophysics and Physics, Enrico Fermi Institute, The University of Chicago, FNAL/NASA Astrophysics Center, Chicago, IL 60637-1433, USA*

Received 10 June 1999; received in revised form 18 August 1999; accepted 4 September 1999

Abstract

An axion detector consisting of a tunable high- Q cavity, a superconducting magnet, and a superheterodyne receiver with an ultra-low noise pre-amplifier has been built to search for galactic halo axions in the mass range of 1.3–13 μeV . The detector instrumentation, search process, and data analysis are described. For the first time, this class of detector has reached sufficient sensitivity to detect halo axions with high confidence. © 2000 Elsevier Science B.V. All rights reserved.

PACS: 14.80M; 95.35; 07.57.K

Keywords: Axions; Dark matter; Microwave detector

1. Introduction

The axion, a hypothetical particle originally proposed in 1977 as a solution to the Strong-CP

problem in QCD [1–6], has a mass which is inversely proportional to the (unknown) energy scale f_a , at which the Peccei–Quinn symmetry is broken:

$$m_a \sim \frac{6 \times 10^{-3}}{f_a} \text{GeV}^2. \quad (1)$$

Not long after its prediction, accelerator- and reactor-based experiments [4] ruled out the existence of an axion corresponding to a symmetry-breaking

*Corresponding author. Tel.: +1-925422-2201; fax: +1-925424-3205.

E-mail address: peng@mitlns.mit.edu, asztalos1@llnl.gov (S. Asztalos)

scale on the order of the electroweak scale ($f_{\text{EW}} \sim 250 \text{ GeV}$) as Peccei and Quinn originally assumed. Subsequent axion models were constructed with $f_a \geq f_{\text{EW}}$, implying axions with extremely small masses and couplings, giving rise to the term “invisible axions”. Astrophysical and cosmological arguments presently constrain the allowed axion mass range to 10^{-6} – 10^{-2} eV . Near the low end of this mass range, axions are produced abundantly in the early universe. The axion contributes to Ω (the ratio of actual energy density in the universe divided the critical density) an amount given by

$$\Omega \sim \left(\frac{m_{\text{a,crit}}}{m_{\text{a}}} \right)^{7/6} \quad (2)$$

where $m_{\text{a,crit}}$ has been estimated [7–14] to be in the range 10^{-6} – 10^{-4} eV . Axions are a form of cold dark matter and as such are one of the leading candidates for constituting the dark matter in galactic halos. Modeling of the Milky Way Galaxy indicates a local halo density of 0.45 GeV/cm^3 [15]. The velocity distribution of the dark matter particles is expected to be approximately Maxwellian with a dispersion of $\sim 270 \text{ km/s}$. There may also be narrow peaks in the velocity distribution due to dark matter particles that have recently fallen into the Galaxy and have yet to thermalize [16].

Since axions in the 10^{-6} – 10^{-2} eV mass range have an extremely weak coupling to ordinary matter and radiation they are exceedingly difficult to detect. However, in 1983 Sikivie showed that even “invisible” axions could be detected using available technology by exploiting the Primakoff effect in which an axion converts to a single real photon in the presence of a magnetic field [17–19]. The coupling for this process is defined as

$$g_{a\gamma\gamma} \equiv g_\gamma \left(\frac{\alpha}{\pi f_a} \right) \quad (3)$$

where g_γ is a model-dependent coupling parameter and α is the electromagnetic coupling constant. For KSVZ [20,21] and DFSZ [5,6] axions, g_γ has a value of -0.97 and 0.36 , respectively. For non-relativistic axions, the energy of the photon is related to the axion mass (ignoring kinetic energy) by the relation

$$hf = m_{\text{a}} c^2. \quad (4)$$

The frequency of the converted photon corresponding to this restricted mass range lies in the microwave region. This led to the construction of a detector based on a tunable microwave resonator cavity permeated by a strong magnetic field. The conversion cross section is resonantly enhanced by the quality factor Q of the cavity. The power resulting from axion-to-photon conversion is currently detected by a low noise High Electron Mobility Transistor (HEMT) pre-amplifier coupled to the cavity. The expected signature of the axion signal is a narrow peak of excess power at the frequency $f = m_{\text{a}} c^2 / h$. The expected width of the signal ($O(10^{-6})$) is due to the virialized motion of galactic axions [15]. In addition, very narrow peaks ($O(10^{-11})$) have been predicted to exist due to the recent capture of extra-galactic axions by the gravitational potential of our galaxy.

Two previous pilot experiments have published results [22–24]. However, neither had the sensitivity to detect halo axions for the expected coupling parameters. The increased sensitivity of the present experiment results from a substantial scale-up of both cavity and magnetic field volume, and improved amplifier noise temperatures. For the first time, this class of detector has achieved sufficient sensitivity [25] to detect KSVZ axions with realistic local axion densities.

2. Detector

2.1. Sensitivity and search rate

The functional requirement for the axion detector is that it convert axions to microwave photons at a power level detectable by currently available technologies. This requirement implies the need to maximize the axion conversion power while minimizing the system noise temperature of the detector. The conversion power level, system noise temperature and averaging time determine the sensitivity and search rate for the experiment.

The axion-to-photon conversion power is governed by the interaction Lagrangian $L = g_{a\gamma\gamma} a \mathbf{E} \cdot \mathbf{B}$, where a is the axion field, \mathbf{B} is the external magnetic field, \mathbf{E} is the cavity electric field, and $g_{a\gamma\gamma}$ is defined above. A configuration suitable for maximizing this

term consists of a large superconducting solenoid and a high- Q microwave cavity. Only low-order TM_{0m0} modes will appreciably couple because they have an electric field component parallel to the magnetic field. However, the conversion power falls rapidly with increasing mode order. Thus the fundamental TM_{010} mode is used exclusively. The conversion power is proportional to the Q -factor of the microwave cavity if the “quality factor” Q_a of the halo axions (the ratio of their total energy to their energy spread) is larger than the cavity Q -factor. This is the case in the present experiment with $Q \approx 10^5$ and $Q_a \approx 10^6$. Furthermore, the conversion power can be enhanced by increasing the cavity volume. A general expression for axion power coupled to the input of the pre-amplifier may be written as

$$P_0 = 1.7 \times 10^{-21} W \left(\frac{V}{0.2\text{m}^3} \right) \left(\frac{B_0}{7.6\text{T}} \right)^2 \times C_{\text{lmn}} \left(\frac{g_\gamma}{0.97} \right)^2 \left(\frac{\rho_a}{7.5 \times 10^{-25} \text{g/cm}^3} \right) \times \left(\frac{f}{700 \text{ MHz}} \right) \left(\frac{Q_L}{90000} \right) \frac{\beta}{(1+\beta)} \frac{1}{1+(2Q_L \delta f/f_0)^2} \quad (5)$$

where V is the volume of the cavity, B_0 is the magnetic field strength at the center of the cavity, ρ_a is the density of galactic halo axions at the Earth, f is the axion frequency, f_0 is the cavity resonant frequency and $\delta f = f - f_0$ specifies the offset from the cavity resonance frequency. The loaded Q -factor Q_L is related to the electric coupling β and unloaded Q -factor Q_0 by $Q_L = Q_0/(1 + \beta)$, C_{lmn} is a mode-dependent form factor [26] given by

$$C_{\text{lmn}} = \frac{\left(\int_V \mathbf{B}(\mathbf{x}) \cdot \mathbf{E}_{\text{lmn}}(\mathbf{x}) d^3\mathbf{x} \right)^2}{B_0^2 V \int_V \varepsilon_r(\mathbf{x}) \mathbf{E}_{\text{lmn}}(\mathbf{x})^2 d^3\mathbf{x}} \quad (6)$$

where $\varepsilon_r(\mathbf{x})$ is the dielectric constant inside the cavity. For the TM_{010} mode in a right circular cylindrical cavity threaded axially by a uniform magnetic field and $\varepsilon_r = 1$, the form factor is 0.69. For a given signal power P_0 , the signal-to-noise

ratio of the detector is determined by the radiometer equation:

$$\text{SNR} = \frac{P_0}{k_B T_s} \sqrt{\frac{t}{B_a}} \quad (7)$$

where T_s is the system noise temperature, t is the integration time, k_B is the Boltzmann constant and B_a is the axion bandwidth. As shown in Eq. (7), the signal-to-noise ratio can, in principle, be enhanced indefinitely by increasing the integration time. Since the cavity has a finite bandwidth, a continuous frequency search is realized by scanning with discrete tuning steps. Using Eqs. (5) and (7), the scanning rate may be written as

$$\frac{df}{dt} \approx \frac{15\text{GHz}}{\text{year}} \left(\frac{V}{0.2\text{m}^3} \right)^2 \left(\frac{B_0}{7.6\text{T}} \right)^4 \times C_{010}^2 \left(\frac{g_\gamma}{0.97} \right)^4 \left(\frac{\rho_a}{7.5 \times 10^{-25} \text{g/cm}^3} \right)^2 \times \left(\frac{f}{700 \text{ MHz}} \right)^2 \left(\frac{Q_L}{90000} \right) \frac{\beta^2}{(1+\beta)^2} \left(\frac{5}{\text{SNR}} \right)^2 \times \left(\frac{3\text{K}}{T_s} \right)^2 \left(\frac{f_{\text{step}}}{\Delta f} \right)^2 \sum_{n=-m}^m \frac{1}{(1 + ((2nf_{\text{step}}/\Delta f))^2)^2} \quad (8)$$

where f_{step} is the frequency interval between successive spectra, Δf the bandwidth of the cavity, and the sum over n refers to the $2m + 1$ spectra which contribute to the signal power at any specific frequency; this quantity is determined by the receiver bandwidth and the scanning step size. From the above expression, the scanning rate is proportional to the ratio $C_{010}^2 Q_L V^2 B_0^4 / T_s^2$. Obviously, it is desirable to maximize these controllable parameters to increase our scanning rate. The present values of V and B_0 (~ 200 l and 7.6 T, respectively) represent a compromise between parameter maximization and cost. On the other hand, the values for Q_L and T_s ($\sim 10^5$ and 3 K, respectively) reflect the limits of our existing copper cavity and HEMT pre-amplifier at LHe temperature.

2.2. Instrumentation

2.2.1. Superconducting magnet and cryostat

The magnet is a simple solenoid with a clear bore diameter of 60 cm, length of 100 cm and a weight of

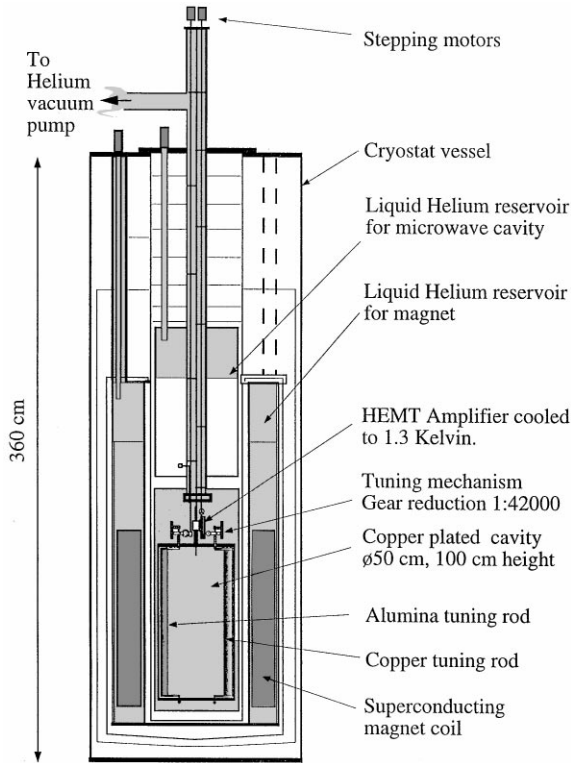


Fig. 1. A drawing of the axion search experiment showing the cryostat and microwave cavity.

6 tons (Wang NMR). It is wound with 106 layers and 37700 turns of NbTi wire in a copper stabilizer. The LHe-cooled coil is mounted near the bottom of a cylindrical cryostat and is surrounded by a LN_2 -cooled radiation shield. The cryostat, shown in Fig. 1 is 3.5 m tall and 1.3 m in diameter. The LHe reservoir above the magnet has a capacity of 400 l.

The magnet itself is divided into four coils of differing superconductor grade to exploit the radial variation in the maximum critical field. Due to the large hoop stresses (1.4×10^4 Mpa, max.) the outer two coils are banded with thin layers of 316 L stainless steel to prevent yielding of the conductors. With an inductance of approximately 500 H, the magnet can be energized to its operating field of $B_0 = 7.6$ T and current of 224 A in about one day at a charging voltage of 3 V. Energizing takes place through permanent vapor-cooled leads consisting of V-shaped longitudinal high-purity copper

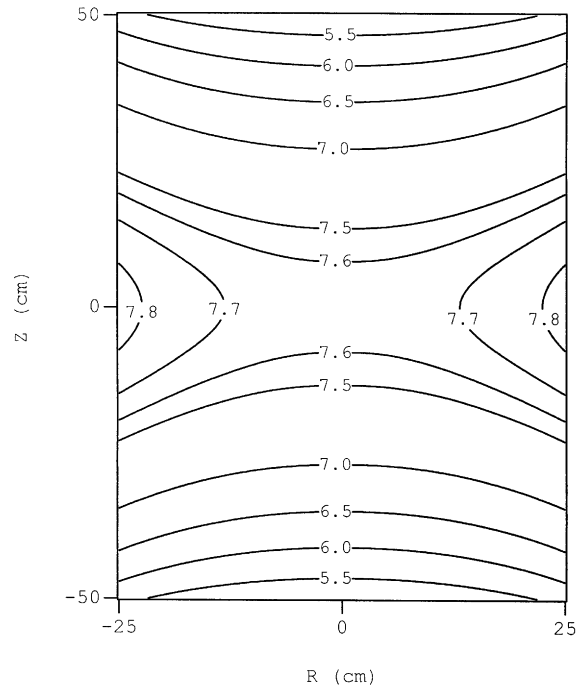


Fig. 2. A contour plot of the calculated total magnetic field (Tesla) in the microwave cavity. Z is distance along the cavity axis and R is the radial coordinate.

pins of cross-sectional area $\sim 0.25 \text{ cm}^2/\text{lead}$ and a length of ~ 1.5 m. A single gas flow tube with a 3" ID contains both current leads which are bolted to central ceramic spacers. At full current the heat load on the inner dewar is 2.5 W, resulting in a LHe boil-off rate of about 2 l/h. A commercial power supply provides the magnet current, which is actively stabilized with a long-term ripple of a few ppm. The control circuit consists of a precision voltmeter (HP 3458A) for reading the magnet current, a digital Proportion-Integration-Differentiation (PID) loop implemented in LabVIEW (National Instruments), and a Digital-to-Analog Converter (HP 59501B) which sets the magnet supply voltage. In our present experiment, the voltage is regulated at ~ 0.3 mV to sustain a B -field of $B_0 = 7.6$ T. Fig. 2 shows the calculated total magnetic field in the cavity. The total stored field energy is 12.7 MJ, which must be safely dissipated. In case of a power outage, the magnet discharges at 6 A/h

through free-wheel diodes at room temperature. An additional quench protection system consisting of a network of resistors and diodes is located on the magnet and provides an alternate current path in case a coil section were to go normal. Under these circumstances, the increased resistance produces a voltage drop across adjacent coils. When the voltage exceeds 5V, the diodes conduct and bring resistors into the circuit. The stored energy in the normal coil is then shared by the remaining superconducting coils via their mutual inductance. The diodes are also designed to isolate the resistors during normal magnet energizing to minimize Helium boil off.

The cryostat has a warm-bore design. The magnet is thermally insulated from the experimental chamber via a vacuum space to minimize heat transfer. This cryostat has a vertical clear bore of 53 cm diameter to allow the experimental vessel containing the microwave cavity and an inner 170 l liquid helium reservoir to be inserted and removed without warming up the magnet. Liquid helium from the reservoir can flow into the cavity area through a heat exchanger and a regulator valve. The valve is operated by a computer controlled stepping motor on the top of the cryostat through a G10 rotary shaft. LHe drips to the bottom of the cavity can, where it replenishes a small reservoir of a few liquid liters, monitored by a level gauge, providing automatic feedback to the valve. A Roots pump maintains a vacuum of ~ 1 Torr at a throughput of ~ 10 l/day. The microwave cavity is usually filled with cold helium vapor. Its temperature is measured by several Cernox thermistors (LakeShore). By regulating the flow of liquid helium into the vessel via the regulator valve, the cavity temperature is maintained at $\sim 1.3 \pm 0.1$ K. The He gas in the cavity and the superfluid ^4He film ensure a uniform temperature of the cavity and tuning rods.

2.2.2. Microwave cavity

The resonant frequency of the microwave cavity depends on the size of the cavity as well as the position of the tuning elements in the cavity. Two sets of microwave cavities have been built to date: (1) A single right-cylindrical cavity, 1 m long and 50 cm in diameter for the frequency range

300–800 MHz, and (2) a pack of four identical cavities, each 20 cm in diameter and 1 m long, for higher frequencies. The cavities were machined from 304 stainless steel and copper plated using the UBAC process (Enthone-OME) with a nominal plated thickness of 0.25 mm. A subsequent annealing step in high vacuum (12 h, 400°C) produces a clean, highly reflective surface finish. Our measured Q values at LHe temperatures were in reasonable agreement with those predicted for copper in the anomalous skin depth regime. At 500 MHz, the empty single cavity unloaded Q in the TM_{010} mode was 65 000 at $T = 300$ K and 290 000 at $T = 4$ K. The electric field profile of TM_{010} with both copper rods midway is shown in Fig. 3. Microwave power is fed to and from the cavities by two semi-rigid coaxial probes protruding into the cavity from the top. One very weakly coupled probe (minor port) is used to inject power for cavity transmission measurements. The second, critically coupled probe (major port, $\beta = 1$), is used to couple power into the pre-amplifier. The major port is maintained at critical coupling by adjusting the probe insertion depth into the cavity. This motion is accomplished with a stepper-controlled linear gear drive mounted above the major port. A springy section of copper coax cable between the

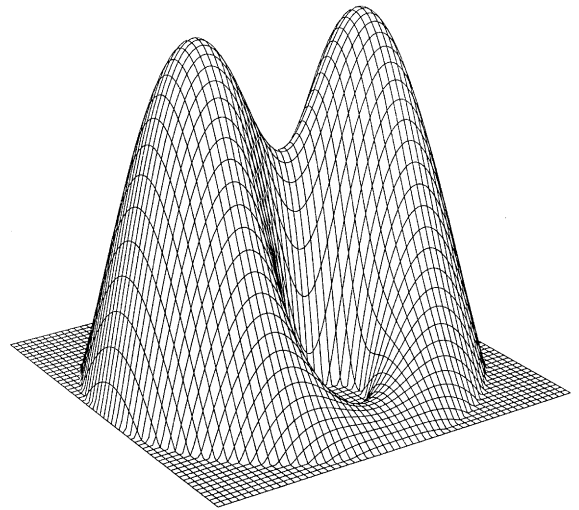


Fig. 3. The E_z field profile of the TM_{010} mode with both copper rods midway.

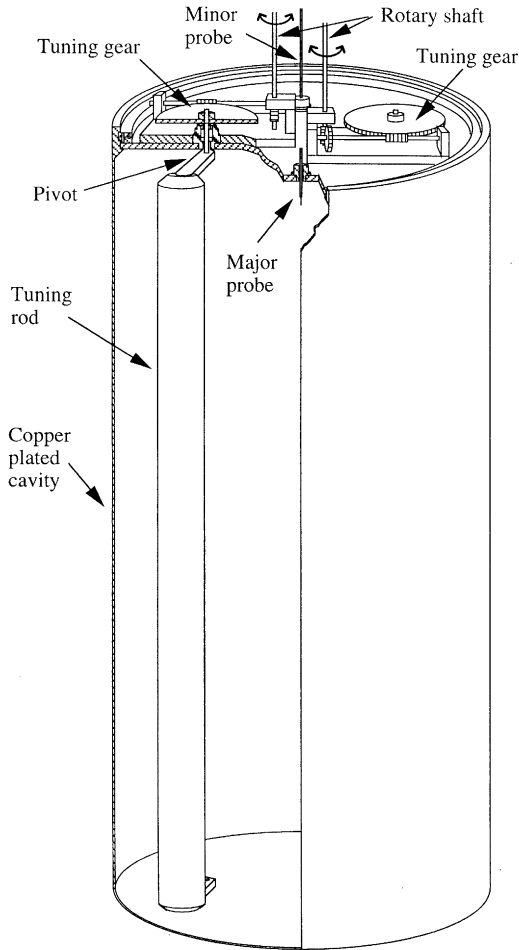


Fig. 4. A cutaway diagram of the single cavity with frequency tuning mechanism.

antenna and the pre-amplifier allows for changing the antenna insertion depth by a few cm.

The tuning mechanism of the single cavity is illustrated in Fig. 4. One or two tuning rods, made of either copper tubing (8 cm diameter) or solid alumina (99.5% pure, 6 cm diameter) can be accommodated. The copper rods consist of tubes and two end caps which are bolted on with recessed screws. All parts were machined from bulk copper, and afterwards copper plated and annealed. The rods are supported by two alumina shafts extending through turrets in the cavity end plates. The support elements for the alumina rods were

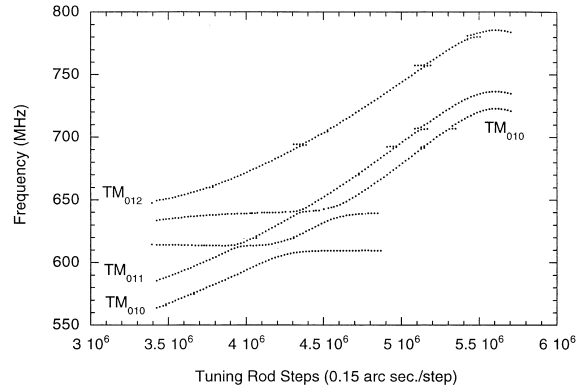


Fig. 5. Mode frequencies of the cavity as functions of tuning steps of one of the metal tuning rods. The other tuning rod is fixed at a position near the cavity wall.

attached with ceramic glue (Aremco, Pyro-Putty 656). A thrust bearing in the top plate supports the tuning rod weight, while an axial bearing in the bottom plate assures vertical alignment. Very small rotations ($\sim 5 \mu\text{rad}$) of the tuning rod about its pivot axis are accomplished with a 2-stage 1:42 000 reduction gear. Each stage consists of a worm gear and an anti-backlash gear. A room temperature stepping motor on top of the cryostat drives the tuning gears through a G10 rotary shaft. There are 8.4×10^6 stepping motor steps per full revolution. A step corresponds to a change in the angle of the tuning rod by 0.15 arcsec. The positioning accuracy of the tuning rod drive is about 1 arcsec.

The radial displacement of either copper or alumina rods within the cavity is accomplished by rotation. Moving a copper rod towards the cavity center shifts the TM_{010} frequency up, whereas moving an alumina rod in that direction shifts it down. Fig. 5 shows the measured frequency tuning curve for the single cavity with two copper rods. Several mode crossings occur where the TM_{010} mode mixes with TEM modes, producing significant holes in the tuning range. In addition, a few smaller holes arise from crossing with TE modes. We take data in holes by filling the cavity with liquid helium at $T = 1.3 \text{ K}$. LHe has a relative dielectric constant $\epsilon_r \sim 1.05$ at $T = 1.3 \text{ K}$, so all mode frequencies are shifted down by $\sqrt{\epsilon_r}$. The

form factor C_{010} was calculated numerically with a 2D finite-difference relaxation technique, while the static magnetic field was calculated from the known coil geometry. The form factor of a cavity tuned with two metal rods is displayed in Fig. 6.

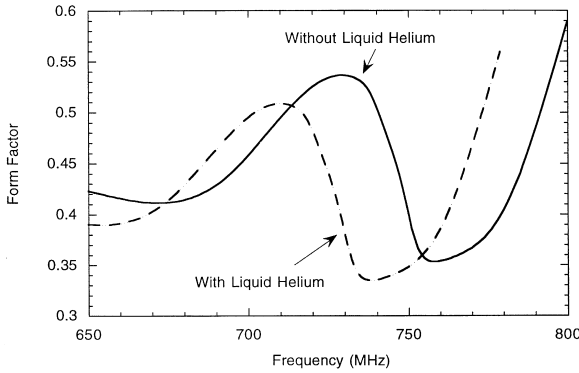


Fig. 6. The form factor of the TM_{010} mode as a function of frequency when the cavity is filled with ~ 1 Torr helium vapor (solid line) and liquid helium (dashed line).

The intrinsic cavity Q -factor is determined by cavity geometry and the losses in the surface of the cavity and copper tuning rods. Dielectric losses are negligible for alumina rods ($\tan \delta < 10^{-7}$) at LHe temperature. Fig. 7 shows the measured loaded

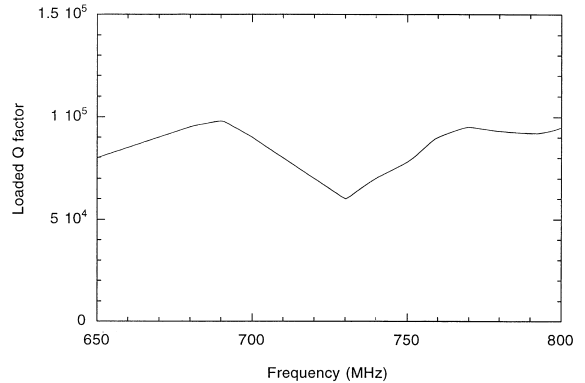


Fig. 7. Measured loaded Q factor of TM_{010} with two copper tuning rods in the cavity.

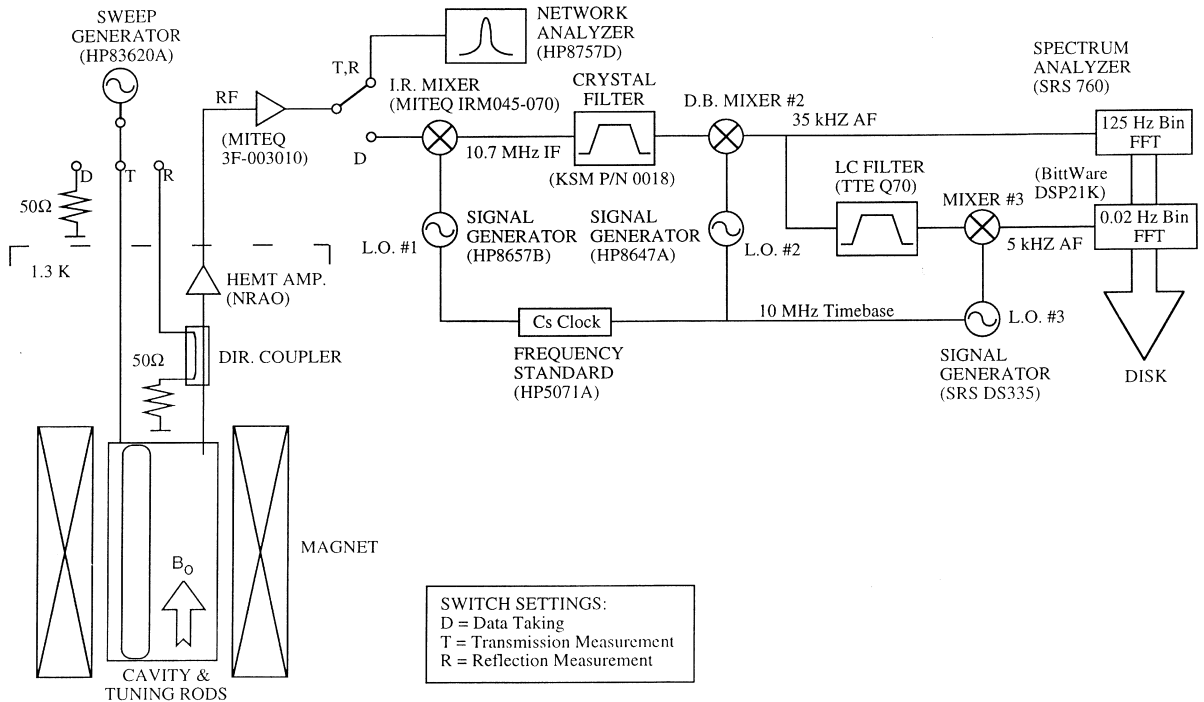


Fig. 8. A schematic diagram of the axion detector microwave electronics.

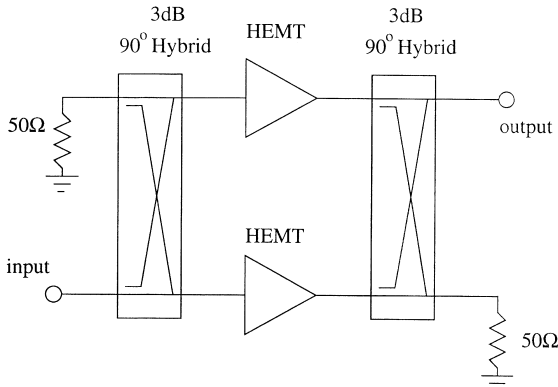


Fig. 9. A schematic diagram of a balanced HEMT amplifier.

Q -factor of the cavity with two copper tuning rods and at critical coupling.

2.2.3. Microwave electronics

The signal processing chain of the detector, depicted in Fig. 8, consists of several amplification and mixing stages. The front-end receiver is a cryogenic HEMT pre-amplifier, built by the National Radio Astronomy Observatory (NRAO). It employs a balanced design, shown in Fig. 9, and has a very low input reflection coefficient over a wide frequency range. The noise temperature is typically 1–2 K (~ 5 K for the first prototype) over a bandwidth of 10–20%, and the power gain is ~ 15 dB. Two such cryogenic amplifiers in series are used in order to overcome the noise from a room temperature post amplifier. An orientation dependence of the amplifier noise temperature in the magnetic fringe field ($B \sim 4$ T) was observed. This is due to a Lorentz force acting on the electrons traversing the HEMT channel and changing its transconductance. Our measurements indicate that this effect can be eliminated by orienting the HEMT channel parallel to the external B field [27].

The cryogenic pre-amplifier is mounted just above the top flange of the cavity so as to minimize the cable length between it and the major probe. The cable length is about 60 cm including the directional coupler. The signal power is coupled out from the cavity to the pre-amplifier through an E -field probe whose insertion depth can be adjusted. The directional coupler (Macom, 2020-

6603-20) between the probe and pre-amplifier allows us to measure the reflection loss and hence the coupling β of the major port. To maximize signal power to the pre-amplifier, the coupling is required to be near critical coupling. The cryogenic amplifiers are followed by a commercial room temperature amplifier (MITEQ 3F-003010) and an image-reject mixer (MITEQ IRM045-070-10.7). The local oscillator (LO) for this mixer is a HP 8657A synthesizer. The intermediate frequency (IF) is set to 10.7 MHz, because both suitable amplification and filtering hardware is available and the LO phase noise is negligible at this frequency. Two IF amplifiers and a temperature-stabilized band-pass crystal filter (KSM Electronics Inc, P/N 0018) of bandwidth 30 kHz are employed. These are followed by a second mixing stage, consisting of a HP 8647 signal generator as LO, and a double-balanced mixer, shifting the cavity signal to a center frequency of 35 kHz. This down-shifted signal is applied to a SRS 760 real-time 400-point FFT spectrum analyzer with a resolution of 125 Hz. These data are referred to as the medium resolution channel. This channel is appropriate for the search for fully thermalized axions $\Delta E/E \sim 10^{-6}$, where the signal would be distributed over ~ 750 Hz width around 700 MHz [15]. It is believed this is the lowest noise temperature receiver ever constructed in this frequency range.

Additionally, the audio signal is fed to a LC bandpass filter with a bandwidth of 4 kHz. The filter output is mixed down to a center frequency of 5.5 kHz and then processed by an ADC/DSP board (BittWare DSP21K) in a PC host computer. A sample of 2^{20} points are obtained with the 16-bit ADC sampling at 20 kHz. Subsequently, a FFT power spectrum yields 2^{19} points with a resolution of 0.02 Hz. These data are referred to as the high resolution channel. This channel is appropriate for the search for fine structure, $\Delta E/E \sim 10^{-11}$, which results from the predicted recent capture of extragalactic axions by the gravitational potential of our galaxy.

2.2.4. Experiment control and data acquisition

Because the axion search experiment is repetitive and operates almost continuously, it was necessary to implement an automated data acquisition

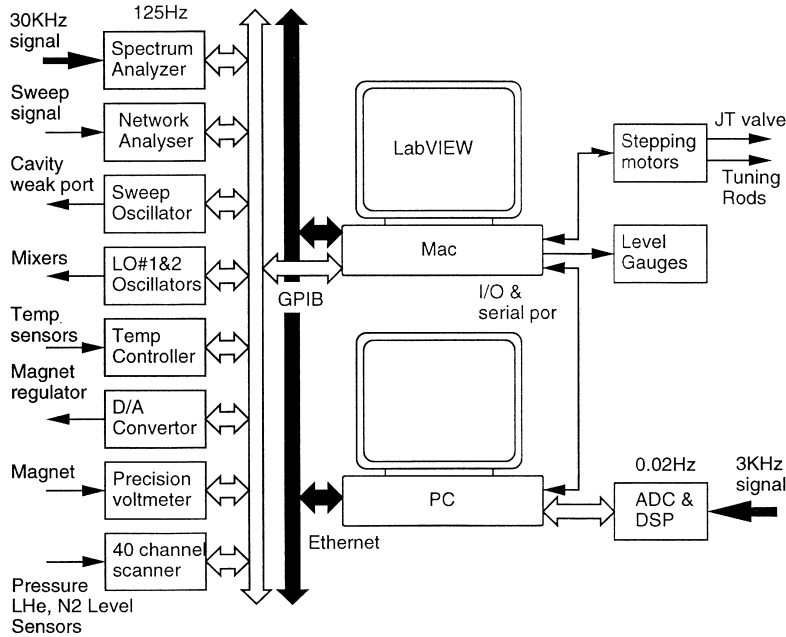


Fig. 10. A block diagram of the computerized instrument control and data acquisition.

system. There are ~ 100 experimental parameters (temperatures, pressures, magnetic field, etc.) to be measured periodically and about a dozen instruments (stepping motors, LO frequency sources, switches) need to be adjusted during each data cycle of 85 s. A data acquisition program (DAQ) routine written in LabVIEW was developed to monitor and control the instruments for data acquisition. The experimental data are saved on disk for off-line analysis. The data are acquired at a rate about 5 MByte/day. During each data acquisition cycle, spectra from the scalar network analyzer, the SRS 760 FFT spectrum analyser and the DSP board are recorded. Finally, the resonance frequency is step-tuned by ~ 2 kHz and the next cycle begins.

The signal flow and control is shown in the block diagram of Fig. 10. The main computer for instrument control and data acquisition is a Apple Macintosh Quadra 950 computer with a GPIB interface (National Instruments) and a digital I/O (National Instruments MIO-16XL) board. A PC Pentium (Gateway) with a ADC/DSP board controls the high-resolution spectrum data acquisition.

Operation of the two computers is coordinated by communication through a serial port. A majority of the instruments are commanded through GPIB, although the stepping motors and level gauges are monitored and controlled through the computer serial ports and digital I/O board, respectively. One of the merits of this experiment is that it can be monitored and controlled remotely over the internet. From an office at MIT in Boston, members of the collaboration can control and monitor the experiment as it runs at Lawrence Livermore National Laboratory in California. The software Timbuktu Pro (Farallon) allows a remote computer to emulate the monitor output and keyboard of the DAQ computer from remote sites.

3. Experiment

In order to minimize systematic errors inherent in a single long averaging time, a strategy of at least two global scans over every frequency point is employed in our experiment. As the frequency step, $f_{\text{step}} \sim 2$ kHz, is much smaller than the receiver

bandwidth (~ 30 kHz), each frequency is covered ~ 15 times per global scan. Covering the same frequency with two or three scans at different times can reduce noise due to transient sources, such as some radio peaks. At present our axion search has employed a single cavity over the frequency range of 500–800 MHz ($2.1 < m_a < 3.3 \mu\text{eV}$), although use of the four-cavity array is set to begin soon.

Besides the raw spectra, experimental parameters are also monitored and measured on-line for each spectrum. These measurements take an additional 4 s to complete. Among the many parameters there are critical ones related to the detector sensitivity including: cavity resonant frequency, loaded Q -factor, electric coupling of the major port, cavity temperature and B -field. The cavity resonant frequency and loaded Q -factor are obtained by measuring the cavity resonance in transmission and fitting it with a Lorentzian curve. The electric coupling of the major port is measured using a reflection method by injecting microwave signals from the coupler port.

To normalize the power spectrum, the transfer function of the receiver must be measured. The transfer function is usually measured over a long integration time (24 h) so that effects of power fluctuations on the normalized spectrum are averaged out. This measurement is made by injecting microwave white noise from a commercial noise source (NoiseCom) into the receiver. Since the transfer function changes slowly, presumably due to aging of the quartz crystals in the crystal filter, such a calibration is required periodically.

The noise temperature of the pre-amplifiers is measured in situ using the Cold-Hot load method around 4.2 K. Here, the cavity acts as a variable temperature noise source as it is warmed up with resistive heaters attached to the top and bottom of the cavity. Prior to warming up the cavity, all liquid helium at the cavity bottom is boiled away. A small amount of helium gas is left in the cavity as a heat exchanger. Since the pre-amplifier has a strong thermal link with the cavity in our detector, the physical temperature of the pre-amplifier also increases. Tests show that the noise temperatures of the NRAO HEMT pre-amplifiers are not significantly changed in the physical temperature range of 1.3–10 K. The change of the gain of the pre-ampli-

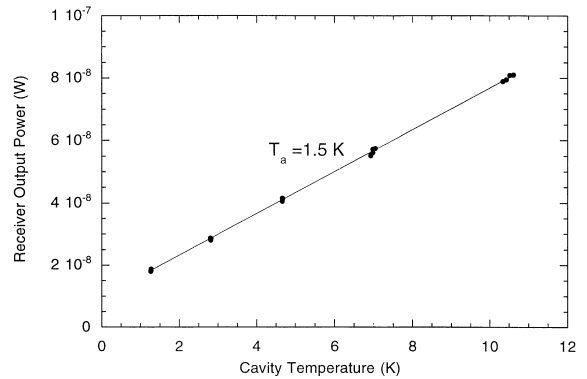


Fig. 11. The pre-amplifier noise temperature is obtained by measuring receiver output noise power as a function of the physical temperature of the cavity.

fier is $< \sim 0.5$ dB. Fig. 11 shows a typical output noise power as a function of the physical temperature of the cavity. It is well approximated by a straight line after the noise power is corrected for the gain change of the pre-amplifier: extrapolating this line down to the temperature axis yields the pre-amplifier noise temperature. Because the NRAO pre-amplifier has a useful bandwidth of ~ 10 –20%, several pre-amplifiers applied to different frequency bands are used in searching for axions over a large mass range.

4. Data processing and analysis

For each frequency point, raw data including experimental status parameters and a power spectrum from the SRS spectrum analyzer is stored on a hard disk for off-line analysis. Each SRS power spectrum consists of 400 frequency bins and each bin is 125 Hz in a fixed frequency window of 10–60 kHz. Fig. 12 shows a typical power spectrum from the SRS 760 spectrum analyzer. The crystal filter causes a rapid falloff in power outside of the bandwidth 20–50 kHz.

In the axion search experiment, unexpected or unwanted changes of experiment parameters such as the cavity temperature and cavity resonator frequency during the period of data acquisition can cause distortions in the FFT power spectrum.

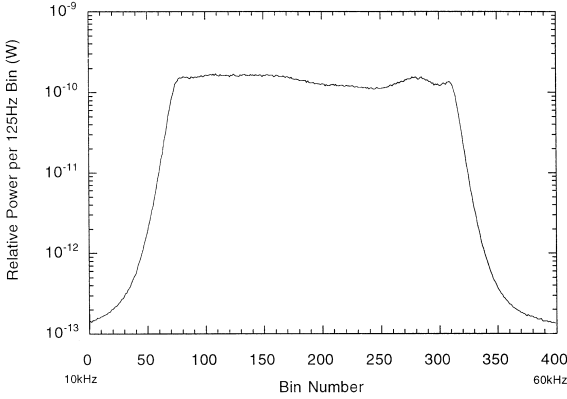


Fig. 12. A typical power spectrum from the SRS 760 spectrum analyzer.

Furthermore, when a mode crossing occurs, the TM_{010} mode becomes hybridized and the form factor degrades. The axion data in this region turns out to be very difficult to analyze. In off-line data pre-processing, those unwanted raw data are eliminated by criteria based on the fluctuation magnitude of the experimental parameters: cavity pressure, cavity temperature, B -field, and cavity frequency shift. The cut does not leave holes in the search because additional scans will cover these frequency ranges. In the experiment, roughly 1–3% of raw data are eliminated and most of these are around the mode crossing areas.

4.1. Noise power and amplifier modeling

A typical power spectrum with receiver transfer function normalization is shown in Fig. 13(a) which is obtained by taking the bin-by-bin ratio of the middle 175 frequency bins (101–275) of the raw spectrum and the receiver transfer function. The Lorentzian shape of the curve is due to a combination of the cavity thermal noise and the amplifier noise reflecting off the cavity coupling [28]. Since there is a finite length of cable between the pre-amplifier and the cavity, the shape of the curve becomes asymmetric and frequency dependent. Fig. 13(b) shows another typical spectrum with a different shape. Such line shapes can be understood using the equivalent circuit model shown in

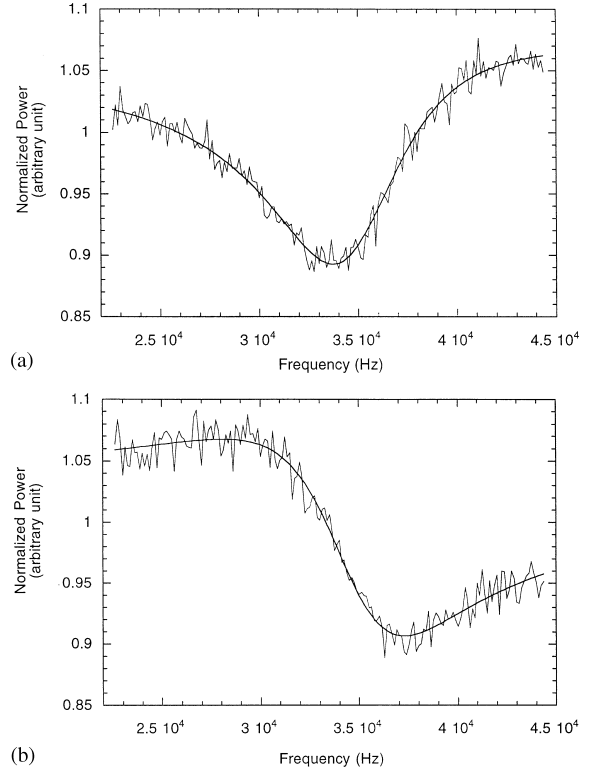


Fig. 13. (a, b). Typical dimensionless spectrum line shapes after the receiver transfer function has been factored out. The solid curves are a fit based on Eq. (9).

Fig. 14. Based on this equivalent circuit, the output noise power of the pre-amplifier may be written as

$$P_{\text{out}} \approx G \times \left(\frac{4k_B T B Z_0^2}{\beta |Z_c(f, \beta) + Z_0|^2} + \frac{|E_n(f) + I_n(f)Z_n(f, \beta, L_0)|^2 Z_0}{|Z_n(f, \beta, L_0) + Z_0|^2} \right) \quad (9)$$

where G is the power gain of the pre-amplifier, k_B is Boltzmann's constant, T is the physical temperature of the cavity, B is the bandwidth, β is the electrical coupling, $E_n(f)$ is the noise voltage of the pre-amplifier, $I_n(f)$ is the noise current of the pre-amplifier, Z_0 is the characteristic impedance, $Z_c(f, \beta)$ is the impedance of the cavity and $Z_n(f, \beta, L_0)$ is the impedance of the cavity with a finite length L_0 of transition cable referred to the input of the pre-amplifier. Fig. 13(a) and (b) also show that the curve fit based on the above amplifier

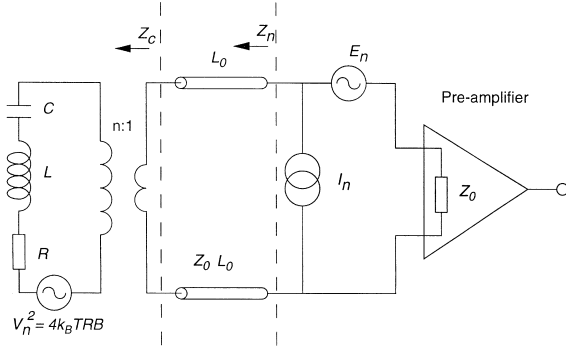


Fig. 14. An equivalent circuit of the cavity and the HEMT pre-amplifier. The length of the cable between the probe and pre-amplifier is L_0 .

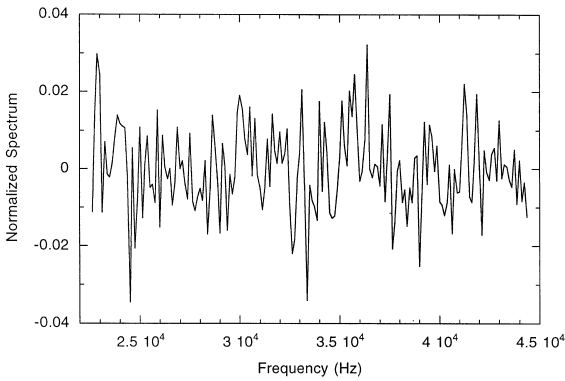


Fig. 15. A typical spectrum after the 5-parameter fit normalization.

and cavity modeling gives a very good agreement with the experimental data. The curve fit is used for obtaining the estimate of the average power of each 125 Hz bin in each spectrum.

4.2. Combining algorithm

After passing a preliminary data cut, the raw data are combined as follows. First, the middle 175 frequency bins of each 400 point spectrum are divided by the corresponding bin of the receiver transfer function. The spectra are then further normalized by the 5-parameter fit curve as discussed above. Fig. 15 shows a single normalized spectrum after the 5-parameter fit normalization. The stan-

dard deviation of bin contents for the dimensionless i th spectrum is defined as

$$\sigma_i = \sqrt{\sum_n \frac{\delta_{ij}^2}{n}} \quad (10)$$

where n is the number of bins and δ_{ij} is the fluctuation about the zero mean of the j th bin in the i th spectrum contributing to the combined data. For a spectrum of purely Gaussian noise, the average value of the standard deviation should be $1/\sqrt{N}$, where N is the number of averages ($N = 10\,000$, for the medium resolution channel). Based on the radiometer Eq. (7), the rms of the noise floor power for each frequency bin is given by

$$\sigma_{ij} = \frac{k_B T_s l_{ij} B}{\sqrt{N}} \approx k_B T_s l_{ij} B \sigma_i \quad (11)$$

where T_s is the noise temperature of the detector including cavity and pre-amplifier noise temperature and l_{ij} is the ratio of the fit function at bin j in the power spectrum to the fit function at the bin coinciding with the cavity resonance. The product $T_s l_{ij}$ describes different noise temperatures for different bins in the same spectrum, the variations of which can be as large as $\sim 20\%$. For our detector, a typical noise power in a single-frequency bin is of the order of 5×10^{-23} W if the noise temperature of the detector T_s is about 3 K, bandwidth B is 125 Hz, and sigma σ_i is about 0.01. The averaging of many spectra thus allows the noise power of each frequency bin to be reduced significantly.

To maximize the signal-to-noise ratio of the combined data, each frequency bin in each spectrum is weighted based on the cavity frequency, Q -factor, mean power of the bin P_{ij} , and the rms of the noise floor power of the bin. The combined fluctuation about the mean power, standard deviation and signal power of the j th bin is given, respectively, by

$$\delta_j = \frac{\sum_i (h_{ij} P_{ij} \delta_{ij}) / \sigma_{ij}^2}{\sum_i (h_{ij} P_{ij}) / \sigma_{ij}^2} \quad (12)$$

$$\sigma_j = \frac{\sum_i (h_{ij}^2 P_{ij}^2) / \sigma_{ij}^2}{\sum_i (h_{ij} P_{ij}) / \sigma_{ij}^2} \quad (13)$$

$$P_j = \frac{\sum_i (h_{ij}^2 P_{ij}^2) / \sigma_{ij}^2}{\sum_i (h_{ij} P_{ij}) / \sigma_{ij}^2} \quad (14)$$

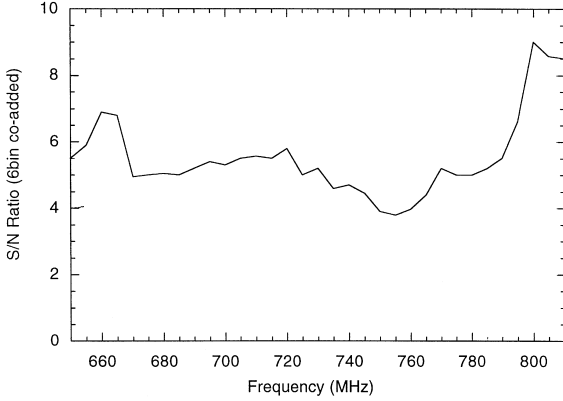


Fig. 16. The signal-to-noise ratio achieved in our axion search for a six bin co-added channel in the frequency range 650–810 MHz.

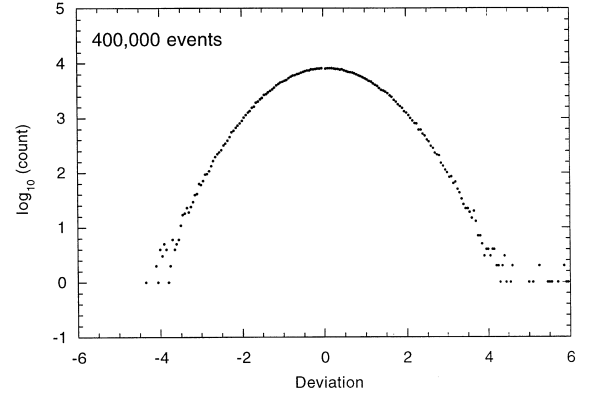


Fig. 17. Typical histogram of the combined data dispersion. The data points describe a quasi-Gaussian distribution.

where the power excess is δ_j , the Lorentzian height h_{ij} is the ratio of axion signal power at the j th bin in the i th spectrum and the maximum axion power bin at resonance peak in the spectrum ($h_{ij} \leq 1$), and the theoretical axion signal power is P_{ij} . In our current axion search, P_{ij} is the signal power of the KSVZ model. The signal-to-noise ratio SNR in the combined data is given by

$$\text{SNR}_j = \sqrt{\frac{\sum_i h_{ij}^2 P_{ij}^2}{\sigma_{ij}^2}}. \quad (15)$$

Fig. 16 shows the signal-to-noise ratio achieved in our axion search for a six-bin co-added analysis over a frequency range of 650–810 MHz. The 6-bin width approximates the expected width of the axion signal. Fig. 17 shows a typical distribution of the combined data which is a quasi-Gaussian distribution. The deviation from a Gaussian distribution of the combined data is mainly caused by the curve fit residuals.

4.3. Monte Carlo simulation

The axion search confidence level is more easily obtained through Monte Carlo simulation because the distribution of the combined data is non-Gaussian after receiver and analysis filtering. To obtain the relation between the confidence level and the

candidate threshold for the combined data, an artificial axion signal with an approximately Maxwellian power distribution and specified power is injected into the raw data [29]. The simulation is briefly described as follows: (1) the real raw-spectrum is normalized using the receiver transfer function and the 5-parameter amplifier-cavity fit. (2) The best fit curve of the spectrum is kept and the normalized real spectrum is discarded. (3) An artificial and normalized spectrum with Gaussian distributed noise of $1/\sqrt{N}$ is created. (4) An artificial axion-like signal at a random set of frequencies is injected (typically the fake signal has a KSVZ power level). (5) The spectrum with the fake signals is multiplied by the fit curve to the raw-spectrum. (6) Finally, the artificial raw-spectrum is combined as was done to the real raw-spectrum. The combined data then contain artificial axion-like signals at known frequencies. By counting the numbers of the injected fake peaks passing the various cut threshold, the relation between the confidence level and the threshold can be obtained. Fig. 18 shows the confidence level or the percentage of the injected fake signals identified in the peak search on the Monte Carlo generated combined data as a function of the candidate threshold. The plot also shows the percentage of noise passing the threshold. These typical curves are the results of the simulation in the frequency range of 800–810 MHz.

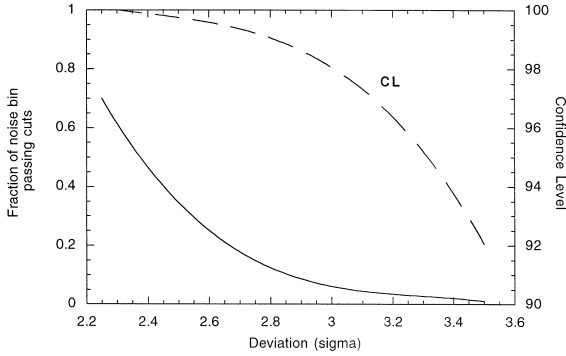


Fig. 18. The confidence level and candidate fraction as functions of the candidate thresholds.

4.4. Exclusion process

Our axion search has four stages from scanning frequency points to establishing exclusion limits. The first stage is the primary scan and associated data processing. The cavity frequency is tuned step-by-step over a wide frequency region. For every frequency region, two or more scans are performed to achieve a signal-to-noise ratio corresponding to our target search confidence level. In the medium resolution channel, a single bin (125 Hz) and 6 bin (750 Hz) co-added bandwidths are examined separately. To achieve a final confidence level of 90% in our current search experiment, a confidence level for the primary scan larger than 90% is required. The typical CL is about 92–93% for the 6 bin co-added channel in the first scan. At this stage, the first axion candidate list is generated for further examination.

At the second stage, only candidates originating from the first axion candidate list are scanned (rescan). The signal-to-noise ratio of the rescan is set to be equal to or larger than the first primary scan and the resulting confidence level is above 99%. Far fewer candidates survive the subsequent cut.

At the third stage, those surviving candidates require a further scan (a persistent candidate scan). At this stage, the confidence level for the cut is set to be above 99%. Usually, only a few candidates survive the persistent candidate scan. Nearly all surviving candidates are found to be strong radio peaks which could be TV or wireless telecommunication signals, etc.

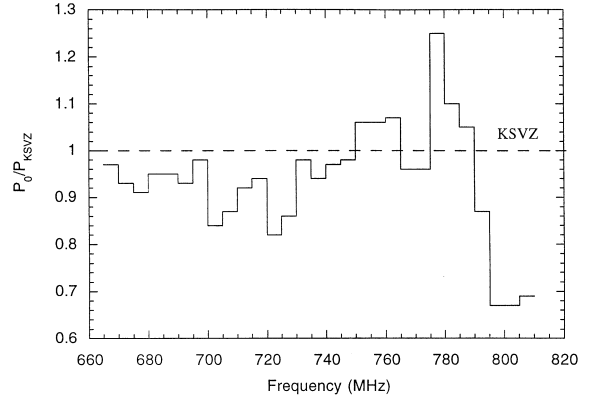


Fig. 19. The axion power P_0 with a ratio above the histogram is excluded with $\sim 90\%$ confidence.

At the fourth stage, the few surviving candidates are examined by terminating the minor port and the couple port where radio signals could couple into the cavity and pre-amplifier. A radio receiver external to the experiment is used to identify those candidates which are strong radio signals. If a candidate still survives the radio peak inspection, final examination would be done by determining whether the persistent candidate survives after ramping down the B -field. Recall that $P_0 \propto B^2$ and thus we can modulate the signal at will. To date, no candidate has required this last verification step.

After this four-stage search, the exclusion limit for the axion can be obtained as the product confidence levels of the various scans. Fig. 19 shows an exclusion plot based on our current axion search around the KSVZ axion power level P_{KSVZ} [29]. Axions with a power ratio above the curve are excluded at the 90% confidence level.

5. Future

To improve the system noise temperature, an ultra-low temperature (100 mK) design based on DC SQUID (Superconducting Quantum Interference Device) amplifiers and a dilution refrigerator is planned. SQUIDS will be used in place of the

HEMT pre-amplifiers. Mück et al. [30] have already demonstrated SQUID amplifiers up to 800 MHz with 10% bandwidth and a gain of ~ 20 dB. Recently, a noise temperature of 0.12 K around 438 MHz and at a physical temperature of $T \approx 0.5$ K was reported. The noise temperature of the SQUID is predicted to drop linearly with temperature down to ~ 100 mK where hot electron effects may become important. If the sensitivity is kept unchanged, the scanning rate would be more than 100 times faster than the current scanning rate. Alternatively, a search for the more weakly coupled DFSZ axion at fractional halo density could be made at the current scanning rate.

To improve the cavity frequency tuning for the cavity operating at mK temperatures, a new type of cryogenic piezo drive for the tuning rods has also been developed. The drive is mounted directly on the top of the cavity eliminating the need for externally driven mechanical gears and stepping motors, thereby cutting down on thermal shorts to the outside. In this design, a ceramic disk fixed on the spindle of the tuning rod is driven by rapid kicks from piezo-elements. This piezo-drive gives tuning resolution that of the current stepping motors.

6. Conclusion

We have developed a halo axion detector using a cryogenic microwave cavity, an ultra-low noise HEMT pre-amplifier and a superheterodyne receiver. A multi-scan search and data processing strategy including a curve fit, combining algorithm, and Monte Carlo simulation have also been developed for improving the signal-to-noise ratio of the detector. For the first time, a detector has reached enough sensitivity to detect KSVZ halo axions with high confidence. An upgrade experiment based on an DC SQUID pre-amplifier is now feasible, which would permit us to search DFSZ model axions, even if they should constitute only a fraction of the halo density.

Acknowledgements

This research is supported by the US. Department of Energy under Contracts No. W-7405-ENG-048, No. DE-AC03-76SF00098, No. DE-AC02-76CH03000, No. DEFG05-86ER40272, No. DE-FC02-94ER40818 and NSF Grant No. PHY-9501959.

References

- [1] R.D. Peccei, H.R. Quinn, Phys. Rev. Lett. 38 (1977) 1440.
- [2] S. Weinberg, Phys. Rev. Lett. 40 (1978) 223.
- [3] F. Wilczek, Phys. Rev. Lett. 40 (1978) 279.
- [4] J.E. Kim, Phys. Rep. 150 (1987) 1.
- [5] M. Dine, W. Fischler, M. Srednicki, Phys. Lett. B 104 (1981) 199.
- [6] A.R. Zhitnitsky, Yad. Fiz. 31 (1980) 497 [Sov. J. Nucl. Phys. 31 (1980) 260].
- [7] J. Preskill, M. Wise, F. Wilczek, Phys. Lett. B 120 (1983) 127.
- [8] L. Abbott, P. Sikivie, Phys. Lett. B 130 (1983) 133.
- [9] M. Dine, W. Fischler, Phys. Lett. B 120 (1983) 137.
- [10] S. Chang, C. Hagmann, P. Sikivie, Phys. Rev. D 59 (1999) 023505.
- [11] R.A. Battye, E.P.S. Shellard, Nucl. Phys. B 423 (1994) 260.
- [12] R.A. Battye, E.P.S. Shellard, Phys. Rev. Lett. 73 (1994) 2954.
- [13] R.A. Battye, E.P.S. Shellard, Phys. Rev. Lett. 76 (1996) 2203.
- [14] M. Yamaguchi et al., Phys. Rev. Lett. 82 (1999) 4578.
- [15] M.S. Turner, Phys. Rev. D. 42 (1990) 3572.
- [16] P. Sikivie et al., Phys. Rev. Lett. 75 (1995) 2911.
- [17] P. Sikivie, Phys. Rev. Lett. 51 (1983) 1415.
- [18] P. Sikivie, Phys. Rev. Lett. 52 (1984) 695.
- [19] P. Sikivie, Phys. Rev. D 32 (1985) 2988.
- [20] J.E. Kim, Phys. Rev. Lett. 43 (1979) 103.
- [21] M.A. Shifman, A.I. Vainshtein, V.I. Zakharov, Nucl. Phys. B 166 (1980) 493.
- [22] S. DePanfilis et al., Phys. Rev. Lett. 59 (1987) 839.
- [23] W. Wuensch et al., Phys. Rev. D 40 (1989) 3153.
- [24] C. Hagmann et al., Phys. Rev. D 42 (1990) 1297.
- [25] C. Hagmann et al., Phys. Rev. Lett. 80 (1998) 2043.
- [26] C. Hagmann et al., Rev. Sci. Instr. 61 (1990) 1076.
- [27] E. Daw, R.F. Bradley, J. Appl. Phys. 82 (4) (1997) 1925.
- [28] E. Moskowicz, J. Rogers, Nucl. Instr. Meth. A 264 (1988) 445.
- [29] E. Daw, Ph.D. Thesis, Massachusetts Institute of Technology, 1998, unpublished.
- [30] M. Mück et al., Appl. Phys. Lett. 72 (1998) 2885.